RSC Advances

COMMUNICATION

View Article Online
View Journal | View Issue

Cite this: *RSC Adv.*, 2015, **5**, 16230

Received 17th January 2015
Accepted 28th January 2015

DOI: 10.1039/c5ra00989h

www.rsc.org/advances

Non-destructive characterization using MCT reveals the composition and distribution of impurities in solar carnallite†

Weijun Song,[ab] Shizhong Yang,[a] Serge Maurice Mbadinga,[a] Xiaoyong Sun[c] and Bozhong Mu*[a]

Micro-computed tomography was applied to investigate impurity composition and distribution in coarse carnallite collected from Qarhan salt lake. The 3-D images suggested that most impurities were concentrated on the crystal surfaces, and the compositions of the impurities were obtained according to the image gray scale and brine constitution.

Carnallite ($KMgCl_3 \cdot 6H_2O$) has been widely used as a feedstock to produce potash fertilizer, metallic magnesium, magnesium oxide and other magnesium compounds.[1] In nature it is usually found in sedimentary deposits of salt ores and solar salts of salt lakes. Carnallite harvested in brine solar evaporation processes was generally found naturally mixed with halite (NaCl), small quantities of sylvite (KCl), impurities of water-insoluble clay, carbonate minerals and anhydrite.[2] Comprehensive knowledge of the impurity particle occurrence modes is essential not only to understand the crystallization and dissolution mechanisms of carnallite but also to optimize the production process. Previous studies have been made to understand the deformation mechanism thermodynamics,[3] kinetics, and processes of carnallite dissolution and crystallization,[4] but the knowledge about impurity occurrence modes on carnallite is still very limited.

Routine crystal detection methods such as X-ray diffraction (XRD), energy dispersive spectrometer (EDS), scanning electron microscope (SEM), atomic force microscope (AFM) and X-ray photoelectron spectroscopy (XPS), *etc.* were difficult to understand crystal inner micro-texture, and most studies focused on micro-chemical analysis of small pieces of materials that were powdered. During testing, the sample must be smashed if crystal size was not small enough and traditional testing techniques could hardly detect *in situ*.

Computer-assisted tomography (CT) was generally used to provide 3-D absorption images of an object from the 2-D images recorded at various angular positions that were processed using appropriate algorithms and software. From the reconstructed 3D data, any virtual slice or perspective renditions of the object can be obtained. When X-ray was at high intensity ($E > 6$ keV), X-ray CT may have an excellent sensitivity so that tiny objects such as cracks, pores and regions that exhibit even a weak (~1%) density variation can be distinguished.[5–9] Micro-computed tomography (MCT) can achieve the resolution in μm range, which is suitable for high precision and small defect detection and be applied to small and medium size specimen. As a result, MCT has been used in many fields.[6,8,10–14] Here we present a nondestructive assay for investigation of the surface morphology and inner density distribution of coarse solar carnallite crystal using MCT, and the constituents of impurities were also estimated by means of image gray scale comparison (see ESI† for the detailed method of comparison).

Our specimen was collected from the solar salt pond of Qinghai Salt Lake Industry Group Co. Ltd, located in Qaidam Basin Qinghai province, northwest of China. The carnallite production flow chart is shown in Fig. S1 (see ESI†). The brine compositions in carnallite pond as well as the brine temperature are also provided.

The specimen was scanned by MCT (Y.CT Precision 1620, YXLON International X-ray GmbH, Germany). The scan parameters were: voltage 150 kV; current 0.20 mA; distances of focus and object to the detector were 850 mm and 817.94 mm, respectively; distance of focus to object was 32.06 mm. CT data were reconstructed as 1024 × 1024 16 bit grayscale images per scan, visualized and analyzed with VG Studio Max 2.2.[7]

In order to show our specimen in different angels, two rotating animations were provided in ESI.† Animation 1 was a raw topography without volume rendering, where the surface topography and the impurities can be observed clearly from different angels. A volume rendering of the impurities is shown

[a]State Key Laboratory of Bioreactor Engineering, Institute of Applied Chemistry, East China University of Science and Technology, Shanghai 200237, P. R. China. E-mail: bzmu@ecust.edu.cn

[b]School of Chemical Engineering, Qinghai University, Xining, 810016, P. R. China

[c]YXLON (Beijing) X-Ray Equipment Trading Co., Ltd, 100081, P. R. China

† Electronic supplementary information (ESI) available. See DOI: 10.1039/c5ra00989h

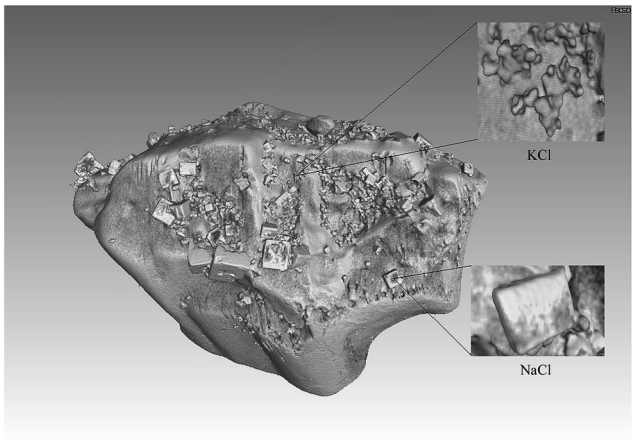

Fig. 1 Typical impurity particles on carnallite.

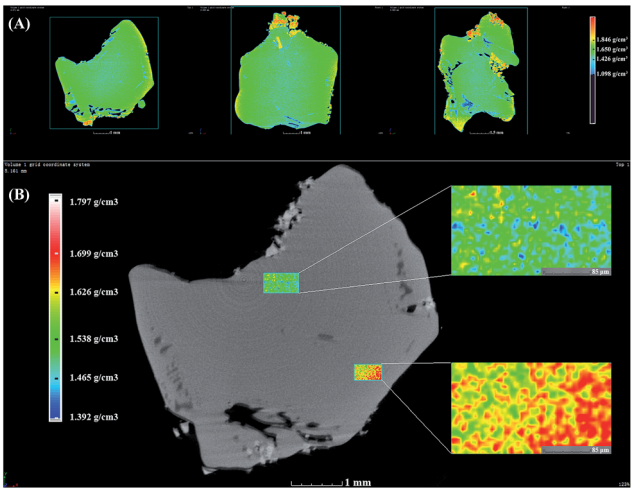

Fig. 2 Inner density distribution CT image of the carnallite, inner density distribution CT image of the carnallite (A) slice image of carnallite crystal, from left to right: in top view, in front view, in right view. (B) A typical slice image from top view which is 5.161 mm to its surface.

in Animation 2, in which the carnallite is rendered in transparency (40%) and impurities are rendered in different colors based on volume. All the impurities volumes are less than 2.5 mm^3 as animation 2 showed. We also provided three slice animations in ESI.† Animations 3–5 were the different slice images from top, front and right angels. As shown in these three animations, little impurities can be seen inside of the specimen.

The relationship between the gray scale ratios of impurities with frequency of their present was displayed in Fig. S3.† As shown in Fig. S3† the range of impurity gray scale ratio distribution were 1.1–1.4, and only a few impurities gray scale ratio was over than 1.4. The main compositions of impurities in crystal carnallite, KCl, NaCl and little $CaSO_4$, were consequently deduced according to the brine compositions and impurity gray scale ratio with carnallite's.[7] Details of the derivation process were showed in ESI.†

The cubic particles, identified as halite (the bigger) and sylvite (the smaller) by gray scale ratio, can be found on the carnallite surface as indicated in Fig. 1. Sylvite existing on carnallite crystal suggested that there may be two possible crystallization processes during brine evaporation: (1) sylvite sedimentation and the carnallite crystallization happen at the same time; and (2) the early precipitation of sylvite particles, suspended in brine, partially dissolves and then adheres on carnallite surface.[15]

Fig. 2A showed the slices from top, right and front views after rendering based on component in an order from left to right. As shown in Fig. 2A that the higher density material was concentrated in an area near the surface and the lower density material was distributed in the center of the crystal. This phenomenon could be explained as follows: (1) nonuniform density distribution inside of crystal might be attributable to the differences of porosity at different positions. At initial stages of the crystallization, due to the higher super-saturation, carnallite crystal growth rate is much higher than that at later stages, thus in the center of crystal, and it is easier to form pores than that in the area near surface. As a result, density of crystal is lower in the center than that in the area near the surface; (2) nonuniform density distribution inside of crystal might also be caused by different K^+ content in different area, near surface K^+ content is much higher than the central area of crystal, and since atomic mass of K^+ was heavier than that of Mg^{2+}, therefore density of carnallite crystal would lower in the central than area near surface. However, further studies are still necessary to verify the conclusions described above.

Fig. 2B showed the crystal inner local density distribution, the slice was in the middle of crystal (distance to surface was 5.161 mm) from top view. We choose two regions to investigate the local density distribution, one region was in the center of crystal and the other one was near the surface. There were many irregular "island" shapes and striations on the slice image as shown in Fig. 2B. It can be observed that the inner local density was nonuniform when CT resolution was 11 μm. The density ranged from 1.392 g cm^{-3} to 1.699 g cm^{-3}. Thus, we postulated that there may be some saturated brine entrained[3] that caused the decline of inner density in blue region. Higher density region appearing in red color is the consequence of crystal structure compact arrangement due to the lower porosity. Above phenomena may provide some helpful ideas to study the growth and dissolution mechanism of carnallite crystal.

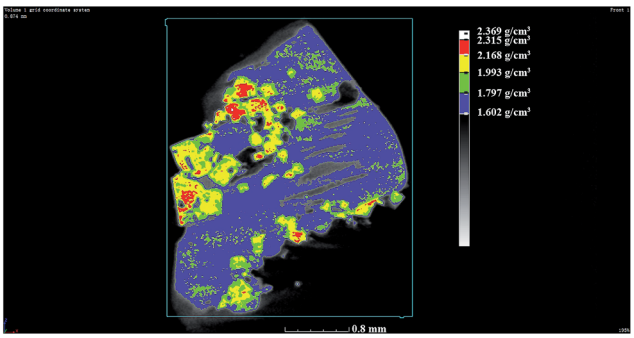

Fig. 3 A slice CT image in front views which was 0.874 mm to surface.

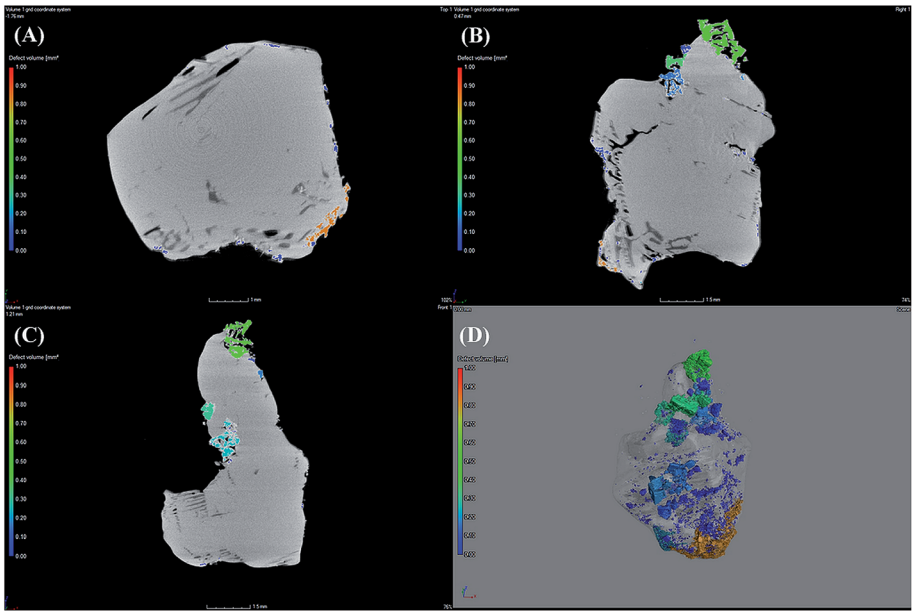

Fig. 4 Impurity distribution CT images rendered in different colors based on particles volume. (A) 2D image of carnallite crystal from top view, (B) 2D image of carnallite crystal from front view, (C) 2D image of carnallite crystal from right view. (D) 3D image of carnallite crystal.

It can be observed in Fig. 3 that the red particles having the highest density (greater than 2.168 g cm^{-3}) were mixed with the cube yellow impurities particles (density above 1.993 g cm^{-3}). The green particles (density greater than 1.797 g cm^{-3}) appeared relatively independently on the surface of crystal. This means that the red particles having the highest density are presumed to be gypsum and not be wrapped in carnallite. On the contrary, they mainly existed in the surface layer mixed with halite. However, $CaSO_4$ was once thought to be entrained in crystals as nuclei of carnallite. According to some prior views, $CaSO_4$ has the lowest solubility and will be precipitated firstly during brine solar evaporation,[16,17] so the earlier formed micro $CaSO_4$ crystals may be the nuclei of other crystals. However, the observed phenomena is in contrast with the previous views and what we observed also confirmed another view which was reported in literature (Zhang *et al.*, 2005) that $CaSO_4$ particles were present independently in coarse carnallite. It can preliminarily conclude that in carnallite main impurities occurrence modes were as follows: the gypsum is mixed with halite and separately existing in the surface layer of carnallite and the halite and the sylvite are embedded in the surface layer of carnallite.

As showed in Fig. 4 that impurities were mainly concentrated on the edge of the slice, which suggested that the impurities were on the surface layer of carnallite. This phenomenon may be explained that different particles contacted and compressed each other during the process of crystallization and then disseminate into the surface layer of each other, alternatively, purities crystal formation at the carnallite surface due to the lower interfacial energy between the purities nucleus and the carnallite surface.

In order to confirm the impurities particles types and the chemical composition, the crystal was smashed for XRD and EDS analysis. The phase structure of carnallite and impurities particles were characterized by XRD, using a Rigaku D/max 2550VB/PC diffractometer with Cu Kα (λ = 0.154 nm) radiation as the incident beam. The components of specimen were semi-quantitatively analyzed by EDS (FALCON, voltage of 15 kV). The XRD patterns and the EDS survey spectra were displayed in Fig. S4 and S5 (ESI†). The diffraction peaks match well with the standard values of carnallite (JCPDS no. 24-0869), halite (JCPDS no. 05-0628) and sylvite (JCPDS no. 41-1476). The EDS survey spectra of the specimen indicate that the crystal main chemical compositions are oxygen, chlorine, magnesium, potassium and sodium. Gypsum cannot be detected maybe because calcium and sulfur concentrations were below the detection limit that the EDS and XRD determine. The results of XRD and EDS characterization proved that the specimen was carnallite with little KCl and NaCl embedded.

Conclusion

The surface morphology, inner structure and density distribution of solar carnallite and impurity compositions were successfully evaluated by using MCT. With this technique, the occurrence, amount and distribution of impurities on carnallite were non-destructively analyzed. In summary, the major impurity constitutions were KCl and NaCl that were mainly embedded on carnallite surface. Additionally, any $CaSO_4$ was hardly entrained inside of solar carnallite. The impurity compositions and occurrence modes detected by MCT were well supported by the data obtained from XRD and EDS.

Acknowledgements

This research has financially supported by the National Natural Science foundation of China (21461021). The authors would

give their thanks to Yuanqin Ma (Qinghai Salt Lake Industry Group Co.) for specimen collection and brine composition data supply.

References

1 V. N. Aptukov, V. Y. Mitin, N. E. Moloshtanova and I. A. Morozov, *J. Min. Sci.*, 2013, **49**, 382–387.
2 S. Titkov, R. Sabirov and N. Panteleeva, *Miner. Eng.*, 2003, **16**, 1161–1166.
3 J. L. Urai, *Tectonophysics*, 1985, **120**, 285–317.
4 P. F. Weck, E. Kim, C. F. Jové-Colón and D. C. Sassani, *Chem. Phys. Lett.*, 2014, **594**, 1–5.
5 F. Mees, R. Swennen, M. Van Geet and P. Jacobs, *Geol. Soc. Am. Bull.*, 2003, **215**, 1–6.
6 H. Zhou, X. H. Peng, E. Perfect, T. Q. Xiao and G. Y. Peng, *Geoderma*, 2013, **195–196**, 23–30.
7 R. A. Ketcham and C. Koeberl, *Geosphere*, 2013, **9**, 1336–1347.
8 E. Herremans, P. Verboven, E. Bongaers, P. Estrade, B. E. Verlinden, M. Wevers, M. L. A. T. M. Hertog and B. M. Nicolai, *Postharvest Biol. Technol.*, 2013, **75**, 114–124.
9 H. Cochard, S. Delzon and E. Badel, *Plant, Cell Environ.*, 2015, **38**, 201–206.
10 P. G. Lutran, K. M. Ng and E. P. Delikat, *Ind. Eng. Chem. Res.*, 1991, **30**, 1270–1280.
11 C. Smith, F. Ahmed, D. Sykes and H. Schroeven-Deceuninck, *EGU General Assembly Conference Abstracts*, 2013.
12 S. R. Du Roscoat, J. Martins, P. Séchet, V. Erwan, P. Latil and C. Geindreau, *Biotechnol. Bioeng.*, 2014, **111**, 1265–1271.
13 S. Peth, C. Chenu, N. Leblond, A. Mordhorst, P. Garnier, N. Nunan, V. Pot, M. Ogurreck and F. Beckmann, *Soil Biol. Biochem.*, 2014, **78**, 189–194.
14 I. Hafsa, B. Cuq, S. J. Kim, A. Le Bail, T. Ruiz and S. Chevallier, *Powder Technol.*, 2014, **256**, 512–521.
15 Z. Jin, H. Zhou and L. Wang, *Chemical Journal of Chinese Universities*, 2001, **22**, 634–638.
16 N. Campbell, K. W. Downes and C. S. Samis, *J. Am. Chem. Soc.*, 1934, **56**, 2507–2512.
17 K. Wallmann, E. Suess, G. Winckler, M. Cita, G. Westbrook and M. Consortium, *Nature*, 1997, **387**, 31–32.